Title

Investigation of iterative image reconstruction in low-dose breast CT

Journal

Physics in Medicine and Biology, 59(11)

ISSN

0031-9155

Authors

Bian, Junguo
Yang, Kai
Boone, John M
et al.

Publication Date

2014-06-07

DOI

10.1088/0031-9155/59/11/2659

Peer reviewed

Published in final edited form as:
Phys Med Biol. 2014 June 7; 59(11): 2659–2685. doi:10.1088/0031-9155/59/11/2659.

Investigation of Iterative Image Reconstruction in Low-dose Breast CT

Junguo Bian,
Department of Radiology, Massachusetts General Hospital & Harvard Medical School

Kai Yang,
Department of Radiology, University of California, Davis

John M. Boone,
Department of Radiology, University of California, Davis

Xiao Han,
Department of Radiology, The University of Chicago

Emil Y. Sidky, and
Department of Radiology, The University of Chicago

Xiaochuan Pan
Departments of Radiology and Radiation & Cellular Oncology, The University of Chicago

Junguo Bian: junguo@pet.mgh.harvard.edu; Kai Yang: kai.yang@ucdmc.ucdavis.edu; John M. Boone: john.boone@ucdmc.ucdavis.edu; Xiao Han: xiaohan@uchicago.edu; Emil Y. Sidky: sidky@uchicago.edu; Xiaochuan Pan: xpan@uchicago.edu

Abstract

Interest exists in developing computed tomography (CT) dedicated for breast-cancer imaging. Because breast tissues are radiation-sensitive, the total radiation exposure in a breast-CT scan is kept low, often comparable to a typical two-view mammography exam, thus resulting in a challenging low-dose-data-reconstruction problem. In recent years, evidence exists suggesting that iterative reconstruction may yield images of improved quality from low-dose data. In this work, based upon the constrained image-total-variation (TV) minimization program and its numerical solver, i.e., the adaptive steepest descent-projection onto the convex set (ASD-POCS), we investigate and evaluate iterative image reconstructions from low-dose breast-CT data of patients, with focuses on identifying and determining key reconstruction parameters, devising surrogate utility metrics for characterizing reconstruction quality, and tailoring the program and ASD-POCS to the specific reconstruction task under consideration. The ASD-POCS reconstructions appear to outperform the corresponding clinical FDK reconstructions, in terms of subjective visualization and surrogate utility metrics.

Correspondence to: Xiaochuan Pan, xpan@uchicago.edu.

I. Introduction

Computed tomography (CT) dedicated for breast-cancer imaging has been a focus of recent investigation [1]–[8]. Current breast-CT prototype scanners employ flat-panel detectors for collecting projection data from the breast at ~500 views over a circular source trajectory, and the FDK algorithm [9], or its variants, is used for reconstructing breast-CT images.

A concern in breast CT is radiation exposure to the breast, because breast tissues are radiation-sensitive [4]. The total radiation exposure in a breast-CT scan thus is kept low, often comparable to a typical two-view mammography exam [4]. When such a low level of exposure is distributed over a large number (~500) of projection views in breast CT, data collected at each view are of low signal-to-noise ratio (SNR). It can thus be challenging to reconstruct images of sufficient spatial and contrast resolutions for detecting calcifications and for discerning and characterizing subtle lesions [10], [11].

In recent years, a great deal of effort has been devoted to the development of iterative image-reconstruction algorithms from low-dose (i.e., low-SNR) data collected in diagnostic CT. There are indications that iterative reconstruction techniques may yield images of improved quality from low-SNR data [12]–[25]. In this work, we investigate and evaluate iterative image reconstructions from low-SNR breast-CT data collected in a clinical trial under a research setting using dedicated breast-CT systems.

II. Basic Materials and Methods

A. Patient-data collection

As described in detail in Ref. [11], the dedicated breast-CT scanner considered employs a flat-panel detector to collect cone-beam projections at 500 views uniformly distributed over 2π of a circular source trajectory. The panel detector consists of 1024×786 effective bins, each of which has a width of 0.388×0.388 mm^2. The source-to-iso-center and the source-to-detector distances were 45.83 cm and 87.78 cm, respectively. Patient data were acquired in a clinical trial for performance evaluation of the breast-CT scanner [26]–[30].

B. Iterative reconstruction

In the reconstruction, an optimization program specifies solutions, whereas iterative algorithms are devised to achieve the designed solutions through solving the optimization program [31]–[47]. In this work, the optimization program and algorithm considered are summarized below.

1) Optimization program—We use vectors **f** and **g** of *N* and *M* entries, respectively, to denote image and data, and design reconstruction **f*** as a solution to the optimization program:

$$\mathbf{f}^{*}=\operatorname{argmin}\|\mathbf{f}\|_{\mathrm{TV}} \quad \text{subject to} \quad D(\mathbf{f})\leq\varepsilon \text{ and } f_j\geq 0, \quad (1)$$

where $\|\mathbf{f}\|_{\mathrm{TV}}$ denotes the image's total variation (TV) [31], [48],

$$D(\mathbf{f}) = \|\mathcal{H}\mathbf{f} - \mathbf{g}\|_2 / M \quad (2)$$

the average Euclidean data divergence, $\mathcal{H}$ the system matrix, f_j the j-th entry of $\mathbf{f}$, and ε a non-negative parameter for controlling the allowable average inconsistency between data and imaging model per detector bin. The optimization program in Eq. (1) is referred to as constrained TV-minimization.

2) Reconstruction algorithms—Algorithms can be developed for image reconstruction through solving the optimization program in Eq. (1). One such algorithm uses adaptively the steepest descent (SD) and projection-onto-the-convex-set (POCS) [49]–[51] to reduce image TV and data divergence, respectively. The algorithm, referred to as the ASD-POCS algorithm [31]–[34], [46], [47], has been demonstrated numerically to solve the constrained TV-minimization in Eq. (1).

The constrained TV-minimization and ASD-POCS algorithm have previously been described in detail [31], [32], [46], [47]. In this work, we investigate and demonstrate their application to reconstructing images from low-SNR breast-CT data.

III. Reconstruction parameters and their determination

A number of reconstruction parameters are needed for a complete specification of the constrained TV-minimization, ASD-POCS algorithm, and thus final reconstructions [32], [46], [47]. We identify below the key reconstruction parameters involved and illustrate their determination in breast-CT applications.

A. Program parameters

For given data $\mathbf{g}$, the complete specification of the constrained TV-minimization in Eq. (1) involves three key parameters: (a) the pixel width[1] (or, equivalently, pixel number N for a given image support); (b) system matrix $\mathcal{H}$; and (c) parameter ε controlling the allowable inconsistency level between data and data model. Their appropriate selection can have a significant impact on reconstruction properties.

1) Pixel width—In general, pixels of small widths may be preferred for possibly yielding sufficient level of spatial and contrast resolutions for detecting micro-calcifications and discerning subtle, low-contrast lesions and normal tissues in breast-CT images. When an image support is given, the smaller the pixel width, the larger the pixel number N (i.e., the entries of $\mathbf{f}$ to be reconstructed). However, M is fixed, and increasing N can result in not only an unrealistic demand on reconstruction time and computation memory, but also a severely under-determined system matrix $\mathcal{H}$ and consequently a reconstruction possibly with significant artifacts. In Sec. VI–A1, we discuss the selection of pixel width.

2) System matrix—System matrix $\mathcal{H}$ plays a key role in specifying the constrained TV-minimization in Eq. (1). For given values of M and N, the property of $\mathcal{H}$ depends upon how

[1]The generalization of the discussion of pixels in 2D to that of voxels in 3D is straightforward.

its elements are actually calculated. For a given scanning geometry, different calculations of the elements can yield $\mathcal{H}$ with different numerical properties. In this work, a standard way was used to calculate an element of $\mathcal{H}$ as the intersection length of an X-ray with a pixel [52], [53].

3) Parameter ε—The specification of the constrained TV-minimization in Eq. (1) involves parameter ε, which sets an upper bound on the allowable discrepancy between data and data model. A larger ε generally permits a larger solution set than does a smaller ε, thus allowing smoother reconstructions with decreased TV. For a given data set and imaging task, methods can be devised for estimating ε [32]–[34]. In Sec. VI–A we describe a scheme based upon an image-power-spectrum metric for estimating ε.

B. Algorithm parameters

Like any algorithm, the ASD-POCS is specified also by algorithmic parameters, including the methods used for reducing data divergence and image TV, and the parameters used for controlling the relative strength between the two reductions [32]–[34]. Different selections of the parameters generally yield different paths hopefully leading to the solutions specified by optimization program.

1) Computation methods—The POCS is efficient in reducing the data divergence of Eq. (2) to close to ε. However, when a convergence is desired, we then switch to the SD method [30], to further reduce data divergence robustly in the neighborhood of ε. Otherwise the SD method for lowering image TV remains unchanged in the ASD-POCS.

2) Additional algorithm parameters—Additional key parameters in the ASD-POCS are described in detail in Ref. [32]: (a) parameter β_{red} controls the update strength in the POCS; and (b) parameters r_{max} and α_{red} balance the reduction strengths in data divergence and image TV. Parameter values similar to those in Refs. [32] were selected, because results of previous and current studies indicate that ASD-POCS with such parameter selections can robustly yield numerically convergent reconstructions according to convergence conditions designed based on Eqs. (3) and (4) below.

C. Convergence parameters

With the program and algorithm parameters discussed, we describe below convergence conditions (or, equivalently, convergence parameters).

1) Convergence conditions—Convergence conditions can be derived for constrained TV-minimization [32]–[34]:

$$D(\mathbf{f}^{(n)}) \to \varepsilon \quad (3)$$

$$c_{\alpha}(\mathbf{f}^{(n)}) \to -1, \quad (4)$$

as iteration number $n \to \infty$, where $\mathbf{f}^{(n)}$ denotes the reconstruction at iteration n, $c_{\alpha}(\mathbf{f}^{(n)})$ is a quantity that can be calculated from $\mathbf{f}^{(n)}$ by use of Eq. (21) in Ref. [32]; and the program

parameter ε is chosen to be above the POCS minimum of $D(\mathbf{f})$, which is larger than, or equal to, the true minimum of $D(\mathbf{f})$. In a practical reconstruction, Eqs. (3) and (4) cannot be satisfied, because a computer has only a finite precision, and because only a finite number of iterations can be performed. Therefore, we form the relaxed convergence conditions: $|\frac{D(\mathbf{f}^{(n)})-\varepsilon}{\varepsilon}| \leq 10^{-4}$ and $|c_\alpha(\mathbf{f}^{(n)}) + 1| \leq 10^{-2}$, for use in this study. When Eqs. (3) and (4) are referred to, we mean the relaxed convergence conditions.

2) Role of iteration numbers—When a convergent reconstruction is of sole interest, its satisfaction of the convergence conditions are the only concern, and the number of iterations required is thus irrelevant. Reconstructions at iterations prior to reaching the convergence, however, can resemble the convergent reconstruction. Moreover, it is not uncommon that, in terms of utility metrics of interest, reconstructions at early iterations may be of some utility, as discussed in Sec. VI. Therefore, if such a reconstruction is of interest, the iteration number becomes a reconstruction parameter; and for different data conditions, a fixed iteration number is likely to yield reconstructions of different levels of image quality.

IV. Algorithm verification and evaluation

A. Algorithm verification

The ASD-POCS and its numerical implementation are first verified in an inverse-crime study [54]–[56], in which a selected $\mathcal{H}$ is used for generating data from a given discrete image (i.e., the truth image), and the same matrix $\mathcal{H}$ is also used in the algorithm for image reconstruction, from the generated data, on the same array of the truth image. We devise an inverse-crime study mimicking the data sampling condition in the breast-CT study, along with convergence conditions tailored specifically to the inverse-crime study below:

$$D(\mathbf{f}^{(n)}) \to 0, \quad (5)$$

$$\mathrm{RMSE}(\mathbf{f}^{(n)}, \mathbf{f}_0) \to 0, \quad (6)$$

$$\mathrm{CTV}(\mathbf{f}^{(n)}, \mathbf{f}_0) \to 0, \quad (7)$$

$$c_\alpha(\mathbf{f}^{(n)}) \to -1, \quad (8)$$

as iteration n increases, where $\mathbf{f}_0$ denotes the truth image, RMSE is the root mean square error between $\mathbf{f}^{(n)}$ and $\mathbf{f}_0$, and $\mathrm{CTV}(\mathbf{f}^{(n)}, \mathbf{f}_0) = |\|\mathbf{f}^n\|_{\mathrm{TV}} - \|\mathbf{f}_0\|_{\mathrm{TV}}|/\|\mathbf{f}_0\|_{\mathrm{TV}}$.

In contrast to Eqs. (3) and (4), the convergence conditions for the inverse-crime study include the following modifications: (a) because the same matrix $\mathcal{H}$ is used for data generation and image reconstruction, the data divergence should be zero, i.e., $\varepsilon = 0$; and (b) because the truth image is known, itself and its TV can both be exploited for devising convergence conditions in Eqs. (6) and (7). An inverse-crime study avoids the selection of

some reconstruction parameters such as pixel width and ε, which are needed in real-data studies.

B. Reconstruction evaluation

A meaningful evaluation of image reconstruction from low-SNR breast-CT data is a non-trivial undertaking because a breast consists of complex, subtle low-contrast textures and because the evaluation should be clinical-task-specific. In general, metrics such as image RMSE and image contrast are inadequate for meaningful assessment of breast-CT reconstruction. Instead, in addition to visual inspection, power-spectrum metrics are devised for evaluating breast-CT reconstruction [57], [58].

1) Visual assessment—Visual inspection offers an important, effective assessment of breast-CT-image reconstruction, even though it may not provide a quantitative result. In real-data studies below, we first perform visual inspection of reconstructed images, focusing primarily on detecting possible artifacts, assessing their overall visual perception, and correlating image visualization to metric-based evaluation result. Visual inspection will also be used for guiding the selection of pixel width in Sec. VI-A1.

2) Power-spectrum metrics—The anatomical power spectrum has been established as a useful tool for characterizing breast-image quality [57], [58]. From a reconstruction, one can calculate its power spectrum $P(k)$, where k is the radial frequency (in units of cyc/mm) in the image-frequency space [33], [58]. It has been shown empirically [58] that $P(k)$ with $0.1 \leq k \leq 0.5$ contains useful texture information in a breast image, that $P(k)$ with $k > 0.5$ hold largely noise and artifact contents, and that the curve $P(k)$ over $0.1 \leq k \leq 0.5$ can be fitted to a power law: $P(k) \propto k^{-\beta}$, where β is the fitted power parameter.

Using knowledge of $P(k)$ (For details how $P(k)$ was calculated, please refer to Sec. 4.3 of Ref. [33].) with $0.1 \leq k \leq 0.5$, we obtain two metrics for evaluation of breast-CT reconstruction: (a) A_p, the area under the power spectrum (AUP) $P(k)$ with $0.1 \leq k \leq 0.5$ and (b) β, a parameter representing the strength and shape of the anatomical power spectrum. It has been found [57] that a smaller β could be correlated to an earlier detection of a growing lesion[2]. As discussed in Sec. VI-A2, metric A_p is used for guiding the selection of ε in real-data studies.

V. Verification: inverse-crime studies

A. Inverse-crime-study design of breast-CT relevance

Without loss of generality, we illustrate below a 2D inverse-crime study: a 2D slice, shown in Fiq. 1a, of a clinical FDK reconstruction on a 380×380 image array from low-SNR breast-CT data is used as the truth image $\mathbf{f}_0$. The use of a clinical image as the truth image allows for the verification study to be of high breast-CT-imaging relevance, because the image contains realistic texture information about breast-tissue. The truth image was used to

[2]The power spectrum result [57] assumes that the image has a shift invariant property and that image noise is a wide-sense stationary stochastic process. Although reconstructed breast-CT images may not strictly satisfy the conditions, we find power-spectrum metrics useful in evaluation of breast-CT images.

generate data at 500 projection views uniformly distributed over 2π for a scanning configuration identical to that of the dedicated breast-CT scanner considered, and the detector used consists of 1024 bins with a width of 0.388 mm in the detector plane.

B. Results of the inverse-crime study

In practical reconstructions, it is unlikely that Eqs. (5)–(8) can be achieved, because of finite computer precision, and because of a finite number of iterations performed. Therefore, using Eqs. (5)–(8), we devise practical convergence conditions: $D(\mathbf{f}^{(n)}) \leq 10^{-8}$, $\text{RMSE}(\mathbf{f}^{(n)}) \leq 10^{-5}$, $\text{CTV}(\mathbf{f}^{(n)}, \mathbf{f}_0) \leq 10^{-3}$, and $|c_\alpha(\mathbf{f}^{(n)}) + 1| \leq 10^{-2}$, and show in Fiq. 2 how the convergence metrics evolve as iteration number n increases.

In Figs. 1b and 1c, we show the numerically convergent reconstruction and its difference with respect to the truth image in Fig. 1a. The results verify (a) that the ASD-POCS can numerically satisfy the convergent conditions, (b) that its computer program is implemented correctly, and (c) that the achieved convergent reconstruction is numerically close to the truth image. Although the inverse-crime study shown is only for a 2D case, it has been carried out for 2D or 3D breast-CT reconstructions, and results and observations similar to those discussed above have been obtained in these additional studies.

VI. Results of Patient-data Studies

In this section, following a demonstration of determination of key reconstruction parameters, we present 2D and 3D reconstructions from breast-CT data.

A. Data-specific determination of reconstruction parameters

All of the reconstruction parameters except for pixel width and ε have been determined in Sec. III, because they are generally robust to data conditions considered. However, as discussed previously, an adequate selection of pixel width and ε can be sensitive to data conditions, and their data-specific determination is illustrated below.

1) Determination of pixel width—We determine an adequate pixel width through performing visual inspection of a series of reconstructions obtained with different pixel widths. For the case considered, its clinical FDK reconstruction with a pixel width of 0.33 mm is displayed in Fig. 3a for a benchmarking purpose, whereas its ASD-POCS reconstruction with pixel width of 0.33 mm is shown in Fig. 3b. To reveal texture details, a zoomed-in view of the selected ROI indicated by the box in the clinical FDK reconstruction is displayed below the corresponding reconstruction. The ASD-POCS reconstruction with a 0.33-mm pixel width in Fig. 3b shows slightly enhanced contrast comparing to that of the clinical FDK reconstruction in Fig. 3a, but some salt-and-pepper artifacts can also be observed. We also considered below reconstructions with pixel widths that are one half (i.e., 0.165 mm) or quarter (i.e., 0.083 mm) of the clinical-FDK-pixel width. For a fair comparison, ASD-POCS reconstructions were converted to the image array of the clinical FDK reconstruction for visualization and for metric calculation. In Figs. 3c or 3d, we show ASD-POCS reconstructions with pixel widths of 0.165 mm or 0.083 mm. Salt-and-pepper artifacts appear to be reduced in the reconstructions, as shown in Figs. 3c or 3d. In fact, inspection of the ASD-POCS images displayed with their actual reconstruction-pixel widths,

which are not shown here, also unveils some under-sampled reconstruction artifacts. This is because, when the pixel width is reduced from 0.33 mm to 0.165 mm or 0.083 mm, the pixel number N increases by 4 or 16 times, thus starting to create issues resulted from under-determinedness in $\mathcal{H}$. However, such artifacts largely diminish when the reconstructions are converted to display on the image array of the clinical FDK reconstruction, leaving with only slight artifacts observed near the skin edge.

For alleviating this issue, we double the data set by including values interpolated from two adjacent rays at each view, resulting in an enlarged data set with an increased M, which is referred to as a doubled-data set. In Fig. 3e, we show the ASD-POCS reconstruction with a 0.165-mm pixel width from the up-sampled data set in which salt-and-pepper artifacts are further reduced. We have also performed ASD-POCS reconstructions with a 0.083-mm pixel width from doubled-data sets and display them in Fig. 3f, which visually resembles the image in Fig. 3e. The additional reconstruction suggests that, for the patient case considered, a pixel dimension smaller than 0.165 mm does not gain in spatial or contrast resolutions, but only with substantially increased cost in computational time and memory. Therefore, we chose the pixel width as one half of that of the clinical FDK reconstruction, along with doubled-data sets, to reconstruct images for all patient cases considered in the work. The Euclidean data divergence at the 200th ASD-POCS iteration is chosen as the ε value in a pixel-width study.

2) Determination of parameter ε—For a given data set, the POCS residual of the Euclidean data divergence is used as the base upon which a set of ε values is selected for ASD-POCS reconstructions. In Fig. 4, we display reconstructions obtained with $\varepsilon = 1.172 \times 10^{-5}$, 1.182×10^{-5}, 1.187×10^{-5}, 1.205×10^{-5}, 1.217×10^{-5}, 1.231×10^{-5}, and observe that, while a small ε yields a noisy reconstruction, an increased ε can, on the other hand, lead to undesirable blocky artifacts in reconstructed images. Conversely, reconstructions with $\varepsilon = 1.182\times10^{-5}$ and 1.187×10^{-5} appear to be near a balance point beyond which breast anatomic information stops, while noise keeps, increasing. This is also confirmed by the quantitative study result below.

We describe below a scheme that employs a power-spectrum metric for quantitatively determining ε. For each selected ε value, we perform an ASD-POCS reconstruction from which the AUP metric, A_p, can be calculated. Conversely, existing studies [58] also suggest that noise content is largely contained in $P(k)$ with $k \geq 0.5$ cyc/mm. Therefore, we calculate another AUP metric, B_p, as the area under the curve $P(k)$ for $0.5 < k \leq 3$ cyc/mm, and employ it as a noise measure in a reconstruction. As ε decreases, A_p rises before leveling out around ε_p, whereas B_p increases continuously, as shown in the top panel of Fig. 5. Furthermore, we have computed the derivatives of A_p and B_p with respect to ε, as depicted in the bottom panel of Fig. 5, to appreciate the variation trends of A_p (i.e., information) and B_p (i.e., noise) as functions of ε. It can be observed that, when ε becomes smaller than ε_p, the derivative of A_p becomes almost zero, whereas the derivative of B_p remains significantly non-zero, suggesting that information stops, while noise keeps, increasing in ASD-POCS reconstructions with ε decreasing to be below ε_p. Therefore, $\varepsilon = 1.187 \times 10^{-5}$ in the neighborhood of ε_p is chosen for yielding an appropriate reconstruction for a given data set. The visual superiority of the reconstruction obtained with the chosen ε is corroborated by

the result in Fig. 4. Based on the results above, we selected ε within the neighborhood of ε_p (near the beginning of the plateau region indicated in the bottom of Fig. 5).

B. Results of breast-CT reconstructions

We have performed image reconstructions from low-SNR breast-CT data and present below reconstructions of three cases representing small-, medium-, and large-size breasts. Using the methods described above, reconstruction parameters were determined for each of the cases. In ASD-POCS reconstructions of 2D or 3D breast-CT images below, one half of the pixel or voxel widths of the corresponding clinical FDK reconstructions were used, along with the corresponding doubled-data sets.

1) 2D breast-CT reconstructions—We discuss first 2D reconstructions of the breasts within the plane containing the circular source trajectory (i.e., the middle plane), thus avoiding potential cone-beam artifacts.

a) Visualization of 2D breast-CT reconstructions: We display in Figs. 6, 7, and 8 clinical FDK (left) and convergent ASD-POCS (right) reconstructions, along with the zoomed-in views of the ROI enclosed by the box, for the three cases. The overall visual appearance for both clinical FDK and ASD-POCS reconstructions are comparable, whereas the latter appear to show enhanced detail, including the calcification within the small breast in Fig. 6. As expected, reconstructions of the large breast appear noisier than the other two cases of smaller breasts. However, some fine details of glandular tissues in the ASD-POCS reconstruction of the large breast appear to be better resolved than those in the corresponding clinical FDK reconstruction. (The wavy background in the large breast images are due to data truncation as a consequence of the breast size is larger than the field of view of the scanner.) The seemingly severer wavy background in the ASD-POCS reconstruction than that in the corresponding clinical FDK reconstruction is the consequence of the more elevated values in FDK images due to data truncation.

b) Characterization of 2D breast-CT reconstructions: Studies suggest a direct correlation between a smaller power-spectrum metric β and an improved lesion-detection performance [57], [59]. Therefore, in addition to visualization inspection, β was calculated from each of the reconstructions and used as a surrogate utility metric for quantitatively characterizing the reconstructions. The β values estimated from the clinical FDK and ASD-POCS reconstructions in Table I indicate that the latter yields β smaller than the former. Studies on additional patient cases are consistent with those shown for the three cases.

c) Evolution of 2D breast-CT reconstructions: It is of practical interest in investigating reconstructions at intermediate iterations. In Figs. 9, 10, and 11, we display ASD-POCS reconstructions at iterations 60 and 80, respectively, for the three cases. Images at the iterations visually resemble their respective convergent reconstructions shown in the right column of Figs. 6, 7, and 8. The power-spectrum metric β calculated from the reconstructions is displayed in Fig 12. It can be observed that β values at iteration number n above 80 are close to those of the convergent ASD-POCS reconstructions, corroborating the

observation on the resemblance of these intermediate reconstructions to their corresponding convergent reconstructions.

2) 3D breast-CT reconstructions—As given by Eq. (4), $c_\alpha(\mathbf{f}^{(\mathbf{n})}) \rightarrow -1$ provides a theoretical, necessary condition for a convergent ASD-POCS reconstruction. Previous studies [32], [46], [47] have shown, however, that ASD-POCS-reconstruction quality, in terms of visualization and various quantitative metrics, remains largely unchanged when $c_\alpha(\mathbf{f}^{(\mathbf{n})})$ becomes lower than −0.6, even before reaching −1. Therefore, a relaxed convergence condition $c_\alpha(\mathbf{f}^{(n)}) \leq -0.6$, instead of Eq. (4), was used for 3D patient-data reconstructions in this work, which requires much fewer iterations than that for achieving the convergence condition in Eq. (4), thus resulting in a considerable saving in computation time.

a) Visualization of 3D breast-CT reconstructions: In Figs. 13, 14, and 15, we display 3D clinical FDK (left) and convergent ASD-POCS reconstructions (right), respectively, within transverse (row 1), coronal (row 2), and sagittal(row 3) slices. The observations similar to those for 2D reconstructions can be made for these 3D reconstructions: the overall visualizations of both clinical FDK and ASD-POCS reconstructions are generally comparable, whereas the latter reveal enhanced details. For example, calcifications with improved contrast in ASD-POCS reconstructions of case 2 can be observed in Fig. 14, and some fine glandular tissue details in the ASD-POCS reconstructions appear to be better resolved than those in the corresponding clinical FDK reconstructions.

b) Characterization of 3D breast-CT reconstructions: We have also calculated the power-spectrum metric β from a stack of 40 transverse slices within the 3D reconstructions, and display the calculation result in Table II. It can be observed that ASD-POCS reconstructions yield β smaller than the corresponding clinical FDK reconstructions. Again, studies on additional patient cases reveal results similar to those of the three cases.

c) Evolution of 3D breast-CT reconstructions: In Figs. 16, 17, and 18, we display ASD-POCS reconstructions at iterations 60 and 80, respectively, for the three cases. Again, images at iterations 60 and 80 appear visually to resemble their corresponding convergent reconstructions shown in the right column of Figs. 13, 14, and 15. The power-spectrum metric β calculated from the reconstructions is displayed in Fig 19, clearly indicating that β values at iteration number n above 80 are already close to those of the convergent ASD-POCS reconstructions, consistent with the observation on the resemblance of these intermediate reconstructions to their respective convergent reconstructions.

VII. Discussion

We have investigated an iterative image reconstruction in low-dose breast-CT imaging. For any reconstruction design and algorithm, multiple parameters are likely to be involved, which can have a significant impact on reconstruction properties and utility. Therefore, the emphasis of this work is placed on (a) tailoring an existing algorithmic framework, i.e., the ASD-POCS, to addressing reconstructions of low-contrast breast images from low-dose patient data, (b) devising surrogate utility metrics (e.g., β) for characterizing reconstruction

quality, and (c) using the surrogate utility metrics for guiding an adequate adaption of the algorithmic framework to the reconstruction task under consideration. Also, patient cases representing a range of breast sizes are considered for characterization of the reconstruction robustness in low-dose breast CT.

For the cases under study, the ASD-POCS reconstructions appear to yield some degree of visual enhancement in terms of spatial and contrast details relative to the corresponding clinical FDK reconstructions, which serve as references. Such an observation is also corroborated by quantitative results of a power-spectrum metric β that has been used as a surrogate utility index for evaluating breast images. However, it should be noted that it remains to be shown as to whether such an "improvement" translates into utility improvement in realistic, clinical applications in which diseases (e.g., calcification cluster or low-contrast tumor,) tasks (e.g., screening or diagnosis,) and observers (e.g., human or computer observers) must also be carefully specified. Clearly, a meaningful evaluation of the clinical utility of ASD-POCS reconstructions for low-dose breast CT needs to be carried out in well-designed studies of specific clinical applications. Such an evaluation is beyond the scope of the current work; however, we are working currently on the design of such studies in which clinically-relevant metrics are being devised for guiding the adaption of iterative reconstructions for a given clinical task.

Depending upon data condition and reconstruction design, the number of iterations can be quite large if the goal is to achieve the designed solution (i.e., the convergent reconstruction) in terms of its numerical satisfaction of the convergence conditions. However, as demonstrated, reconstructions at early iterations, before reaching the convergent reconstruction, may highly resemble, visually and quantitatively, the former. Therefore, from a practical point of view, reconstructions at early iterations can be of practical utility.

When the data-SNR level is low, reconstruction of breast-CT images can be challenging. Because the total imaging exposure is approximately proportional to the product of the projection-view number and X-ray flux at each projection view. For a given amount of total exposure radiation, the data-SNR level at each view can be increased through the reduction of the view number. It is perhaps of practical interest to investigate how, for a given amount of total exposure radiation, a trade-off between view numbers and X-ray flux per view would affect reconstruction "quality" in breast-CT imaging.

Acknowledgments

The authors would like to thank Dr. Ingrid Reiser for helpful discussions. This work was supported in part by the National Institutes of Health (NIH) under Grants R01s CA120540, EB000225, EB002138, and CA158446.

References

1. Chang CHJ, Sibala JL, Fritz SL, Dwyer SJ III, Templeton AW. Specific value of computed tomographic breast scanner (CT/M) in diagnosis of breast diseases. Radiology. 1979; 132:647–652. [PubMed: 472242]
2. Gisvold JJ, Reese DF, Karsell PR. Computed tomographic mammography (CTM). Am J Roentgenol. 1979; 133:1143–1149. [PubMed: 116508]

3. Chang CHJ, Nesbit DE, Fisher DR, Fritz SL, Dwyer SJ III, Templeton AW, Lin F, Jewell WR. Computed tomographic mammography using a conventional body scanner. Am J Roentgenol. 1982; 138:553–558. [PubMed: 6978009]
4. Boone JM, Nelson TR, Lindfors KK, Seibert JA. Dedicated breast CT: Radiation dose and image quality evaluation. Radiology. 2001; 221:657–667. [PubMed: 11719660]
5. Chen B, Ning R. Cone-beam volume CT breast imaging: Feasibility study. Med Phys. 2002; 29:755–770. [PubMed: 12033572]
6. Boone JM, Shah N, Nelson TR. A comprehensive analysis of DgN(CT) coefficients for pendant-geometry cone-beam breast computed tomography. Med Phys. 2004; 31:226–235. [PubMed: 15000608]
7. Brzymialkiewicz CN, Tornai MP, McKinley RL, Bowsher JE. Evaluation of fully 3-d emission mammotomography with a compact cadmium zinc telluride detector. IEEE Trans Med Imag. 2005; 24:868–877.
8. Glick SJ. Breast CT. Annu Rev Biomed Eng. 2007; 9:501–526. [PubMed: 17506654]
9. Feldkamp LA, Davis LC, Kress JW. Practical cone-beam algorithm. J Opt Soc Am A. 1984; 1:612–619.
10. Xia JQ, Lo JY, Yang K, Floyd CE Jr, Boone JM. Dedicated breast computed tomography: Volume image denoising via a partial-diffusion equation based technique. Med Phys. 2008; 35:1950–1958. [PubMed: 18561671]
11. Lindfors K, Boone J, Nelson T, Yang K, Kwan A, Miller D. Dedicated Breast CT: Initial Clinical Experience1. Radiology. 2008; 246(3):725–733. [PubMed: 18195383]
12. Thibault JB, Sauer KD, Bouman CA, Hsieh J. A three-dimensional statistical approach to improved image quality for multislice helical CT. Med Phys. 2007; 34:4526–4544. [PubMed: 18072519]
13. Beister M, Kolditz D, Kalender WA. Iterative reconstruction methods in X-ray CT. Phys Medica. 2012; 28:94–108.
14. Hara AK, Paden RG, Silva AC, Kujak JL, Lawder HJ, Pavlicek W. Iterative reconstruction technique for reducing body radiation dose at CT: feasibility study. Am J Roentgenol. 2009; 193:764–771. [PubMed: 19696291]
15. Silva AC, Lawder HJ, Hara A, Kujak J, Pavlicek W. Innovations in CT dose reduction strategy: application of the adaptive statistical iterative reconstruction algorithm. Am J Roentgenol. 2010; 194:191–199. [PubMed: 20028923]
16. Singh S, Kalra MK, Hsieh J, Licato PE, Do S, Pien HH, Blake MA. Abdominal CT: comparison of adaptive statistical iterative and filtered back projection reconstruction techniques. Radiology. 2010; 257:373–383. [PubMed: 20829535]
17. Leipsic J, LaBounty TM, Heilbron B, Min JK, Mancini GJ, Lin FY, Taylor C, Dunning A, Earls JP. Adaptive statistical iterative reconstruction: assessment of image noise and image quality in coronary CT angiography. Am J Roentgenol. 2010; 195:649–654. [PubMed: 20729442]
18. Pontana F, Pagniez J, Flohr T, Faivre JB, Duhamel A, Remy J, Remy-Jardin M. Chest computed tomography using iterative reconstruction vs filtered back projection (part 1): evaluation of image noise reduction in 32 patients. Eur Radiol. 2011; 21:627–635. [PubMed: 21053003]
19. Singh S, Kalra MK, Gilman MD, Hsieh J, Pien HH, Digumarthy SR, Shepard JAO. Adaptive statistical iterative reconstruction technique for radiation dose reduction in chest CT: a pilot study. Radiology. 2011; 259:565–573. [PubMed: 21386048]
20. Gervaise A, Osemont B, Lecocq S, Noel A, Micard E, Felblinger J, Blum A. CT image quality improvement using adaptive iterative dose reduction with wide-volume acquisition on 320-detector CT. Eur Radiol. 2012; 22:295–301. [PubMed: 21927791]
21. Kalra MK, Woisetschläger M, Dahlström N, Singh S, Digumarthy S, Do S, Pien H, Quick P, Schmidt B, Sedlmair M, et al. Sinogram-affirmed iterative reconstruction of low-dose chest CT: effect on image quality and radiation dose. Am J Roentgenol. 2013; 201:W235–W244. [PubMed: 23883238]
22. Yu L, Leng S, Chen L, Kofler JM, Carter RE, McCollough CH. Prediction of human observer performance in a 2-alternative forced choice low-contrast detection task using channelized

hotelling observer: Impact of radiation dose and reconstruction algorithms. Med Phys. 2013; 40:041908. [PubMed: 23556902]

23. Deák Z, Grimm JM, Treitl M, Geyer LL, Linsenmaier U, Körner M, Reiser MF, Wirth S. Filtered back projection, adaptive statistical iterative reconstruction, and a model-based iterative reconstruction in abdominal CT: an experimental clinical study. Radiology. 2013; 266:197–206. [PubMed: 23169793]
24. Miéville FA, Berteloot L, Grandjean A, Ayestaran P, Gudinchet F, Schmidt S, Brunelle F, Bochud FO, Verdun FR. Model-based iterative reconstruction in pediatric chest CT: assessment of image quality in a prospective study of children with cystic fibrosis. Pediatr Radiol. 2012:1–10.
25. Hoxworth J, Lal D, Fletcher G, Patel A, He M, Paden R, Hara A. Radiation dose reduction in paranasal sinus CT using model-based iterative reconstruction. Am J Neuroradiol. 2013:1–6.
26. Boone JM, Seibert JA. Monte carlo simulation of the scattered radiation distribution in diagnostic radiology. Med Phys. 1988; 15:713–720. [PubMed: 3185407]
27. Kwan ALC, Boone JM, Shah N. Evaluation of X-ray scatter properties in a dedicated cone-beam breast CT scanner. Med Phys. 2005; 32:2967–2975. [PubMed: 16266111]
28. Yang, K. PhD dissertation. University of California Davis; 2007. Development and Evaluation of a Dedicated Breast CT Scanner.
29. Glover GH. Compton scatter effects in CT reconstructions. Med Phys. 1982; 9:860–867. [PubMed: 7162472]
30. Bian, J. PhD dissertation. The University of Chicago; 2012. Optimization-based Image Reconstruction from a Small Number of Projections.
31. Sidky EY, Kao CM, Pan X. Accurate image reconstruction from few-views and limited-angle data in divergent-beam CT. J X-Ray Sci and Technol. 2006; 14:119–139.
32. Sidky EY, Pan X. Image reconstruction in circular cone-beam computed tomography by constrained, total-variation minimization. Phys Med Biol. 2008; 53:4777–4807. [PubMed: 18701771]
33. Bian J, Siewerdsen JH, Han X, Sidky EY, Prince JL, Pelizzari CA, Pan X. Evaluation of sparse-view reconstruction from flat-panel-detector cone-beam CT. Phys Med Biol. 2010; 55:6575–6599. [PubMed: 20962368]
34. Han X, Bian J, Eaker DR, Kline TL, Sidky EY, Ritman EL, Pan X. Algorithm-enabled low-dose micro-CT imaging. IEEE Trans Med Imag. 2011; 30:606–620.
35. Li M, Yang H, Kudo H. An accurate iterative reconstruction algorithm for sparse objects: application to 3D blood vessel reconstruction from a limited number of projections. Phys Med Biol. 2002; 47:2599–2609. [PubMed: 12200927]
36. Ritschl L, Bergner F, Fleischmann C, Kachelrieß M. Improved total variation-based CT image reconstruction applied to clinical data. Phys Med Biol. 2011; 56:1545–1561. [PubMed: 21325707]
37. Ramirez-Giraldo JC, Trzasko J, Leng S, Yu L, Manduca A, McCollough CH. Nonconvex prior image constrained compressed sensing (NCPICCS): Theory and simulations on perfusion CT. Med Phys. 2011; 38:2157–2167. [PubMed: 21626949]
38. Defrise M, Vanhove C, Liu X. An algorithm for total variation regularization in high-dimensional linear problems. Inverse Probl. 2011; 27:065002.
39. Rashed EA, Kudo H. Statistical image reconstruction from limited projection data with intensity priors. Phys Med Biol. 2012; 57:2039–2061. [PubMed: 22430037]
40. Lauzier PT, Tang J, Chen GH. Prior image constrained compressed sensing: Implementation and performance evaluation. Med Phys. 2012; 39:66–80. [PubMed: 22225276]
41. Lee H, Xing L, Davidi R, Li R, Qian J, Lee R. Improved compressed sensing-based cone-beam CT reconstruction using adaptive prior image constraints. Phys Med Biol. 2012; 57:2287–2307. [PubMed: 22460008]
42. Sidky EY, Pan X, Reiser IS, Nishikawa RM, Moore RH, Kopans DB. Enhanced imaging of microcalcifications in digital breast tomosynthesis through improved image-reconstruction algorithms. Med Phys. 2009; 36:4920–4932. [PubMed: 19994501]
43. Sidky E, Anastasio M, Pan X. Image reconstruction exploiting object sparsity in boundary-enhanced X-ray phase-contrast tomography. Opt Express. 2010; 18:10 404–10 422. [PubMed: 20173816]

44. Sidky EY, Duchin Y, Pan X. A constrained, total-variation minimization algorithm for low-intensity X-ray CT. Med Phys. 2011; 38:S117–S125. [PubMed: 21978112]
45. Xia D, Xiao X, Bian J, Han X, Carlo EYSFD, Pan X. Image reconstruction from sparse data in synchrotron-radiation-based microtomography. Rev Sci Instrum. 2011; 82(4):043706. [PubMed: 21529012]
46. Han X, Bian J, Ritman EL, Sidky EY, Pan X. Optimization-based reconstruction of sparse images from few-view projections. Phys Med Biol. 2012; 57:5245–5273. [PubMed: 22850194]
47. Bian J, Wang J, Han X, Sidky EY, Shao L, Pan X. Optimization-based image reconstruction from sparse-view data in offset-detector CBCT. Phys Med Biol. 2013; 58:205–230. [PubMed: 23257068]
48. Chambolle A. An algorithm for total variation minimization and applications. J Math Imaging Vis. 2004; 20:89–97.
49. Gordon R, Bender R, Herman GT. Algebraic reconstruction techniques (ART) for three-dimensional electron microscopy and X-ray photography. J Theor Biol. 1970; 29:471–481. [PubMed: 5492997]
50. Youla DC, Webb H. Image restoratoin by the method of convex projections: Part 1 – theory. IEEE Trans Med Imag. 1982; 1:81–94.
51. Combettes PL. The foundations of set theoretic estimation. Proc IEEE. 1993; 81:182–208.
52. Joseph PM. An improved algorithm for reprojecting rays through pixel images. IEEE Trans Med Imag. 1982; 1:192–196.
53. Siddon RL. Fast calculation of the exact radiological path for a three-dimensional CT array. Med Phys. 1985; 12:252–255. [PubMed: 4000088]
54. Colton, DL.; Kress, R. Inverse acoustic and electromagnetic scattering theory. Springer-Verlag; Berlin: 1992.
55. Wirgin A. The inverse crime. arXiv:math-ph/0401050v1. 2004
56. Kaipioa J, Somersalob E. Statistical inverse problems: discretization, model reduction and inverse crimes. J Comput Appl Math. 2007; 198:493–504.
57. Burgess AE, Jacobson FL, Judy PF. Human observer detection experiments with mammograms and power-law noise. Med Phys. 2001; 28:419–437. [PubMed: 11339738]
58. Metheany KG, Abbey CK, Packard N, Boone JM. Characterizing anatomical variability in breast CT images. Med Phys. 2008; 35:4685–4694. [PubMed: 18975714]
59. Chen L, Abbey CK, Boone JM. Association between power law coefficients of the anatomical noise power spectrum and lesion detectability in breast imaging modalities. Phys Med Biol. 2013; 58:1663–1681. [PubMed: 23422272]

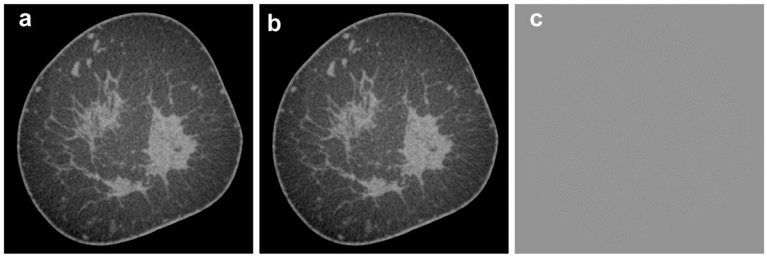

Figure 1.

(a) Truth image, (b) the ASD-POCS reconstruction, and (c) difference between the truth image and the ASD-POCS reconstruction, in the inverse-crime study. The display windows for (a) and (b) is [0.15, 0.25] cm^{-1} and for (c) is $[-1.0 \times 10^{-4}, 1.0 \times 10^{-4}]$ cm^{-1}, respectively.

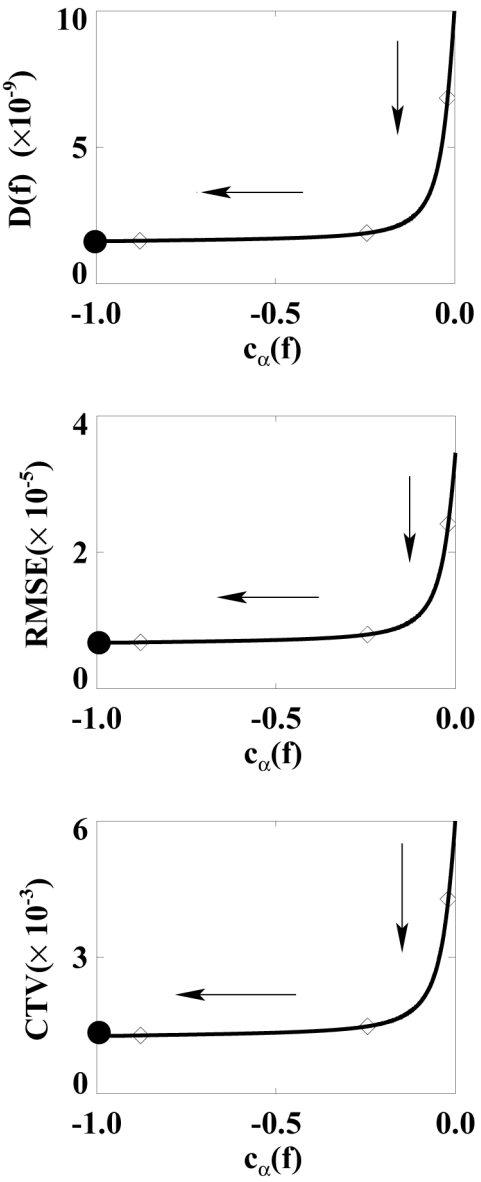

Figure 2.

Evolution of convergence metrics as the iteration number increases in the inverse-crime study: $D(\mathbf{f}^{(n)})$ (top), RMSE($\mathbf{f}^{(n)}$, $\mathbf{f}_0$) (middle), and CTV($\mathbf{f}^{(n)}$, $\mathbf{f}_0$) (bottom) as functions of $c_\alpha(\mathbf{f}^{(n)})$. The arrows in the plots indicate the increasing direction of the iteration number, the three "◇" (right to left) indicate points at iterations 2000, 4000, and 6000, whereas the solid circs denote the designed solution.

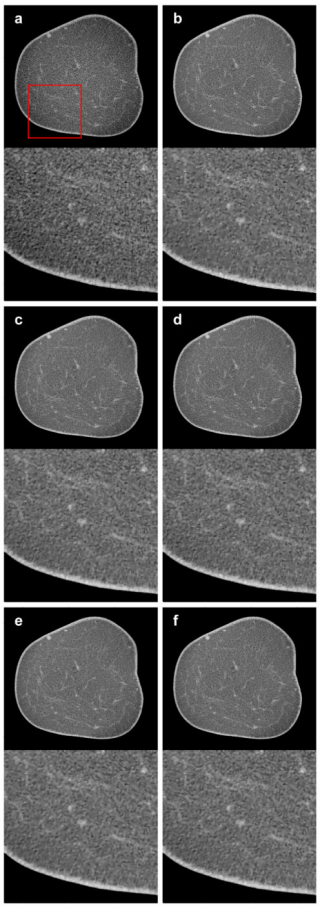

Figure 3.

Clinical FDK reconstruction (a); ASD-POCS reconstructions, from the original data, with pixel widths that are (b) the same as, (c) one half of, and (d) a quarter of that of the clinical FDK reconstruction; and ASD-POCS reconstructions, from doubled-data, with pixel widths that are one half (e) and a quarter (f) of that of the clinical FDK reconstruction. Beneath each of the reconstructions, we display the corresponding zoomed-in view of the ROI within the box depicted in (a). The display window is [0.15, 0.25] cm^{-1}.

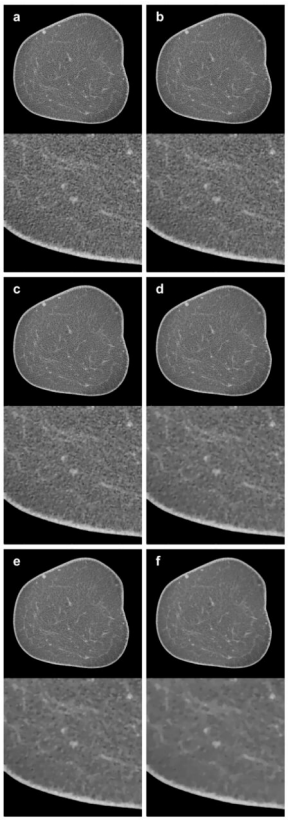

Figure 4.

ASD-POCS reconstructions with (a) $\varepsilon = 1.172 \times 10^{-5}$, (b) 1.182×10^{-5}, (c) 1.187×10^{-5}, (d) 1.205×10^{-5}, (e) 1.217×10^{-5}, and (f) 1.231×10^{-5}. Beneath each of the reconstructions, we display the corresponding zoomed-in view of the ROI within the box depicted in Fiq. 3a. The display window is [0.15, 0.25] cm^{-1}.

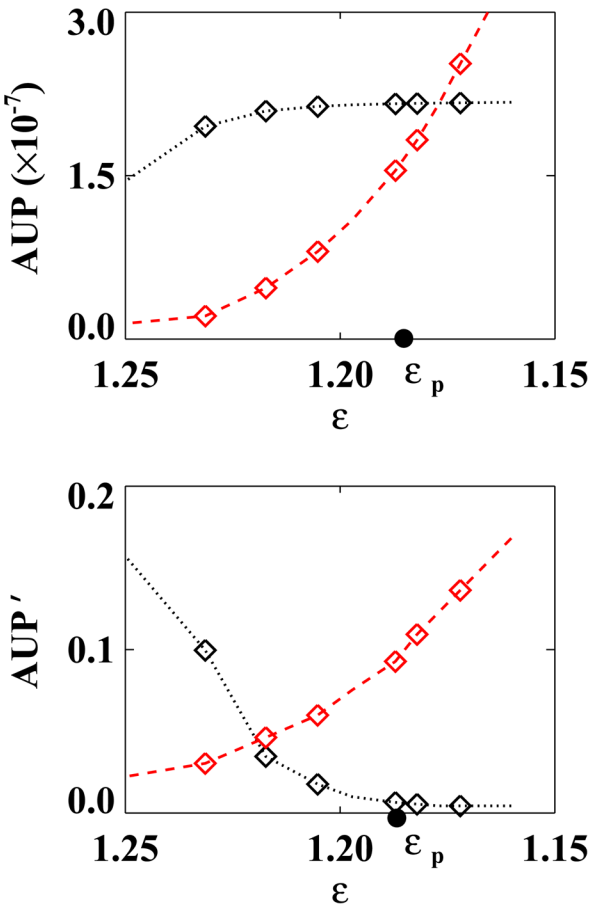

Figure 5.

(Top) A_p (dotted) and B_p (dashed) with an arbitrary unit, and (bottom) their respective derivatives as functions of ε ($\times 10^{-5}$). ASD-POCS reconstructions with ε values of data points denoted by "◇" are shown in Fiq. 4. Also, ε_p denotes the neighborhood where the derivative of A_p levels out to become zero. B_p in the top plot was scaled up for illustration convenience.

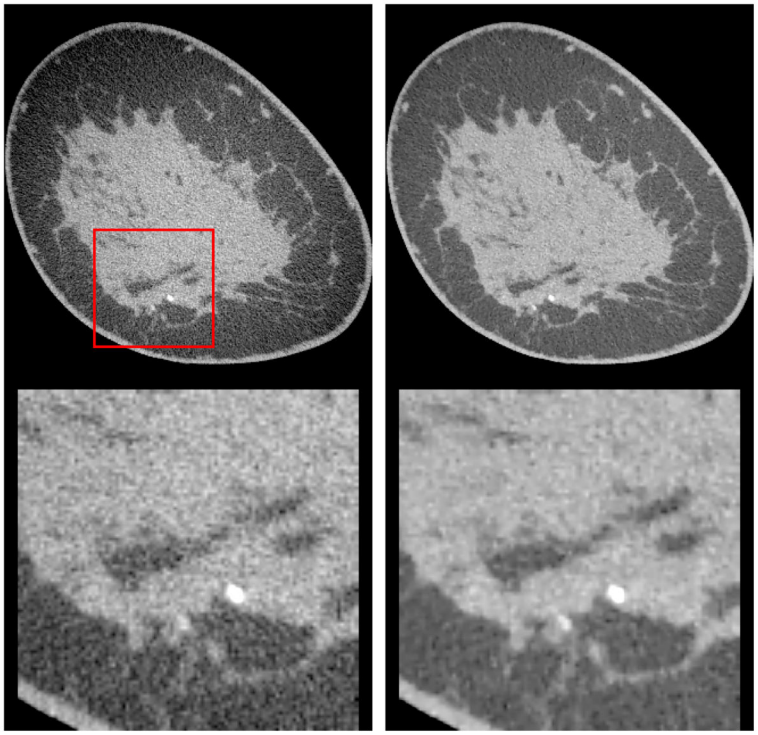

Figure 6.

Clinical FDK (left) and ASD-POCS (right) reconstructions for a small-size breast (case 1). Beneath each of the reconstructions, we display the corresponding zoomed-in view of the ROI within the box depicted in the clinical FDK reconstruction. The display window is [0.15, 0.25] cm^{-1}.

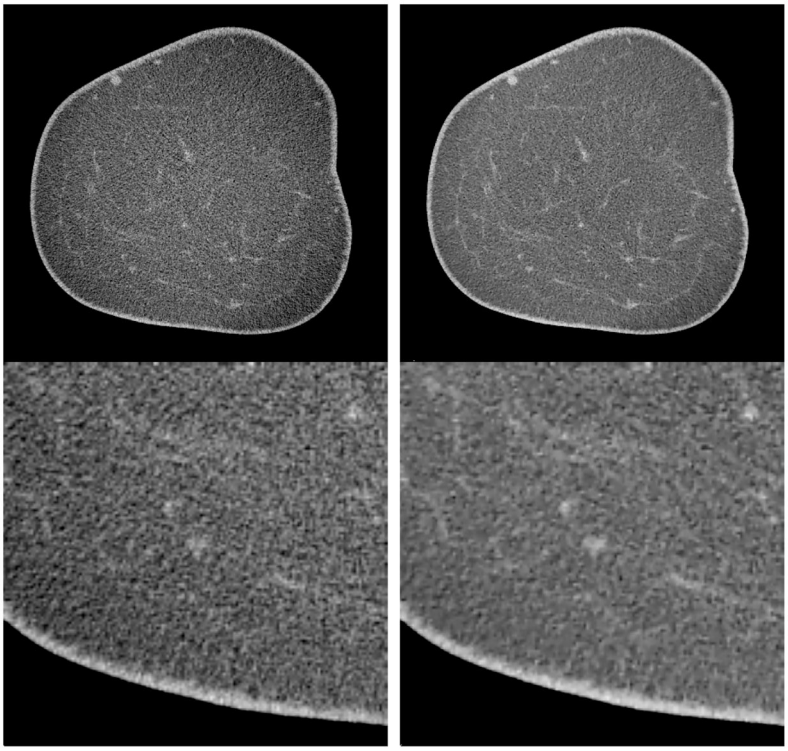

Figure 7.

Clinical FDK (left) and ASD-POCS (right) reconstructions for a medium-size breast (case 2). Beneath each of the reconstructions, we display the corresponding zoomed-in view of the ROI within the box depicted in Fig. 3a. The display window is [0.15, 0.25] cm^{-1}.

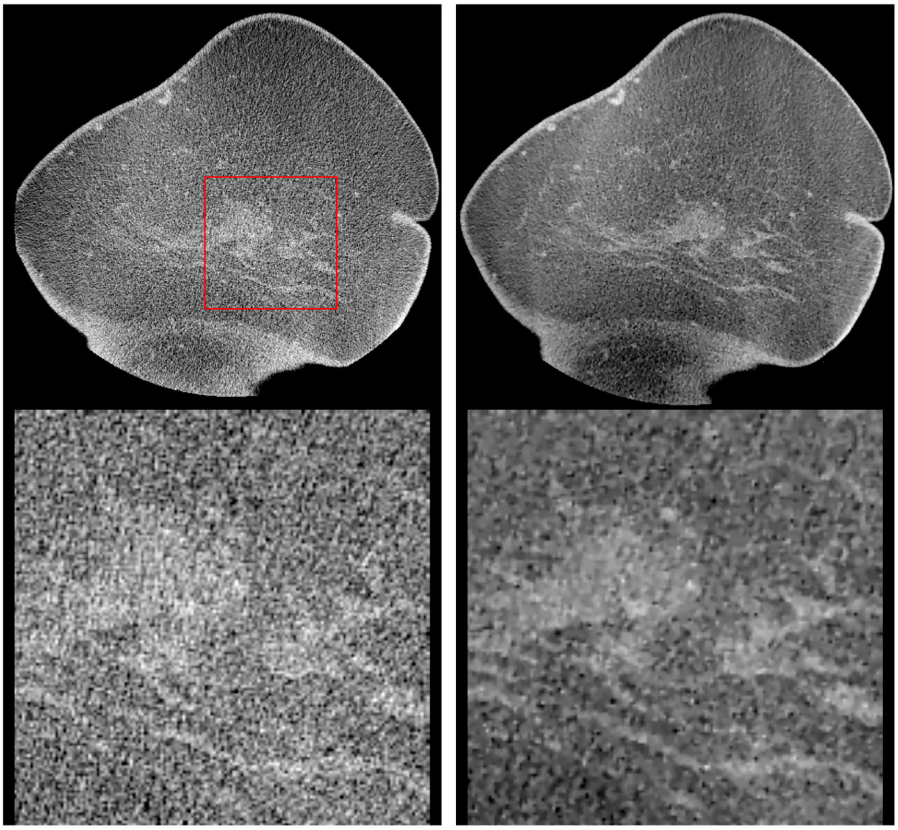

Figure 8.

Clinical FDK (left) and ASD-POCS (right) reconstructions for a large-size breast (case 3). Beneath each of the reconstructions, we display the corresponding zoomed-in view of the ROI within the box depicted in the clinical FDK reconstruction. The display window is [0.15, 0.25] cm^{-1}.

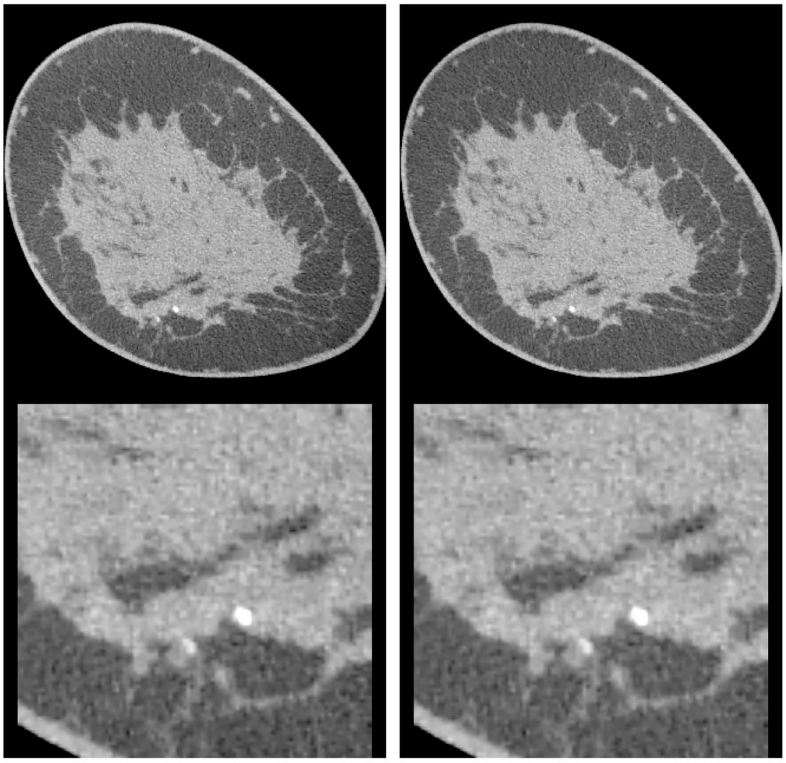

Figure 9.

ASD-POCS reconstructions at iterations 60 (left) and 80 (right) for the small-size breast. Beneath each of the reconstructions, we display the corresponding zoomed-in view of the ROI within the box depicted in the clinical FDK reconstruction of Fiq. 6. The display window is [0.15, 0.25] cm^{-1}.

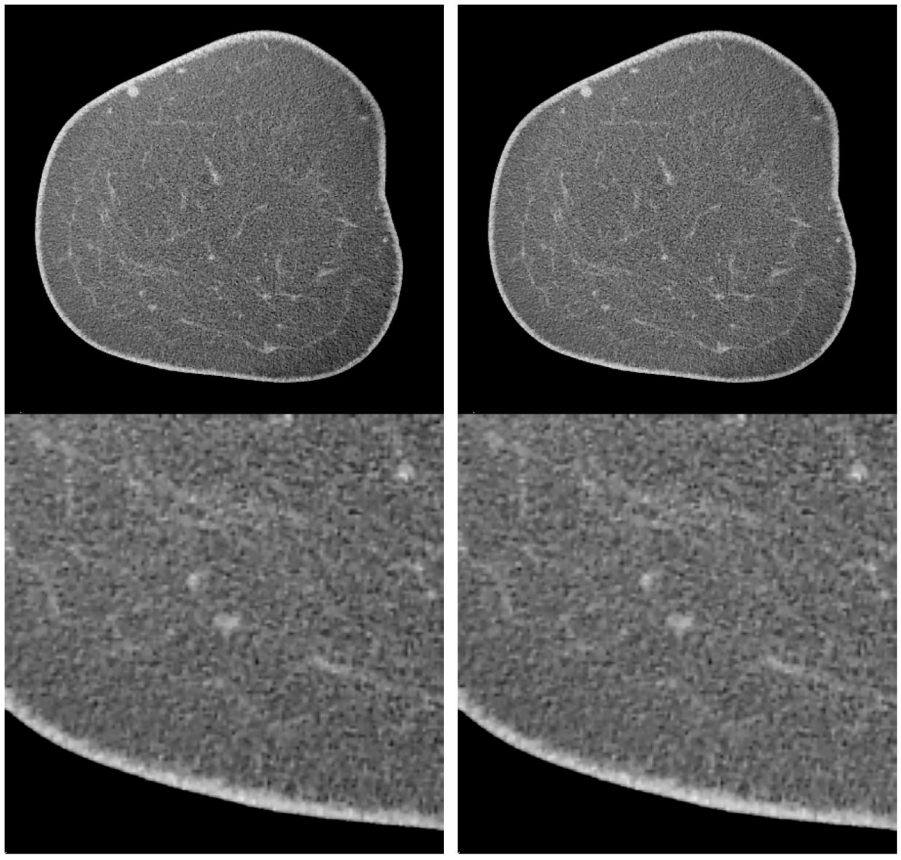

Figure 10.

ASD-POCS reconstructions at iterations 60 (left) and 80 (right) for the medium-size breast. Beneath each of the reconstructions, we display the corresponding zoomed-in view of the ROI within the box depicted in Fiq. 3a. The display window is [0.15, 0.25] cm^{-1}.

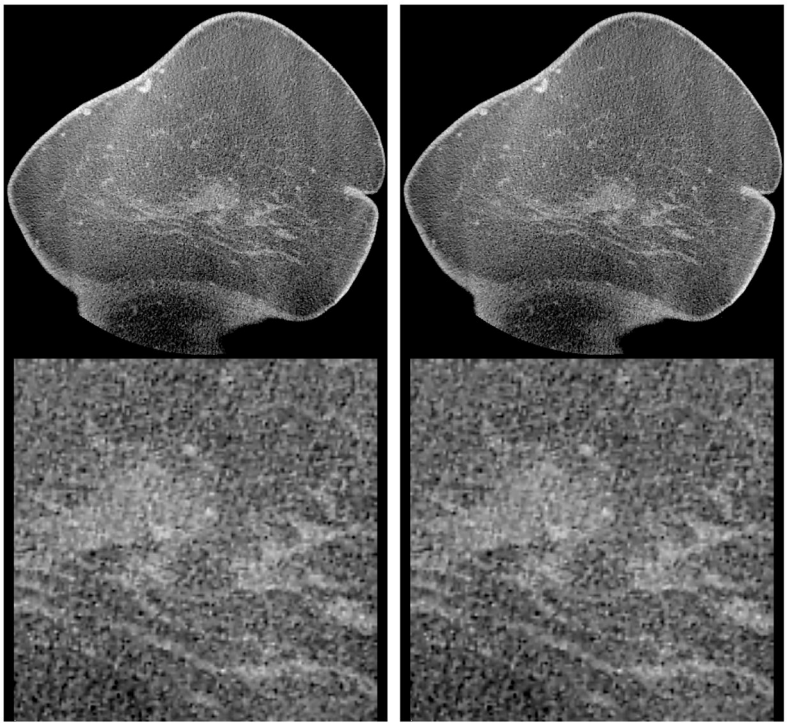

Figure 11.

ASD-POCS reconstructions at iterations 60 (left) and 80 (right) for the large-size breast. Beneath each of the reconstructions, we display the corresponding zoomed-in view of the ROI within the box depicted in the clinical FDK reconstruction of Fiq. 8. The display window is [0.15, 0.25] cm^{-1}.

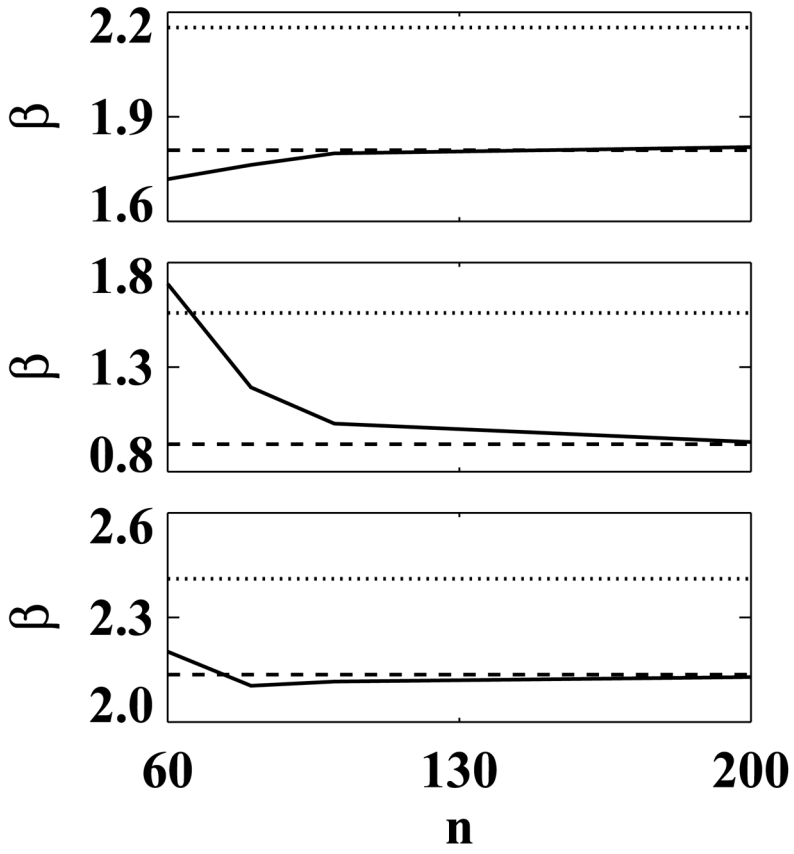

Figure 12.

Power-spectrum metric β as functions of iteration number n, along with those estimated from the convergent ASD-POCS reconstructions (dashed), for small- (row 1), medium- (row 2), and large-size (row 3) patient breast cases. Values of β estimated from the corresponding clinical FDK images (dotted) are plotted as benchmarking references.

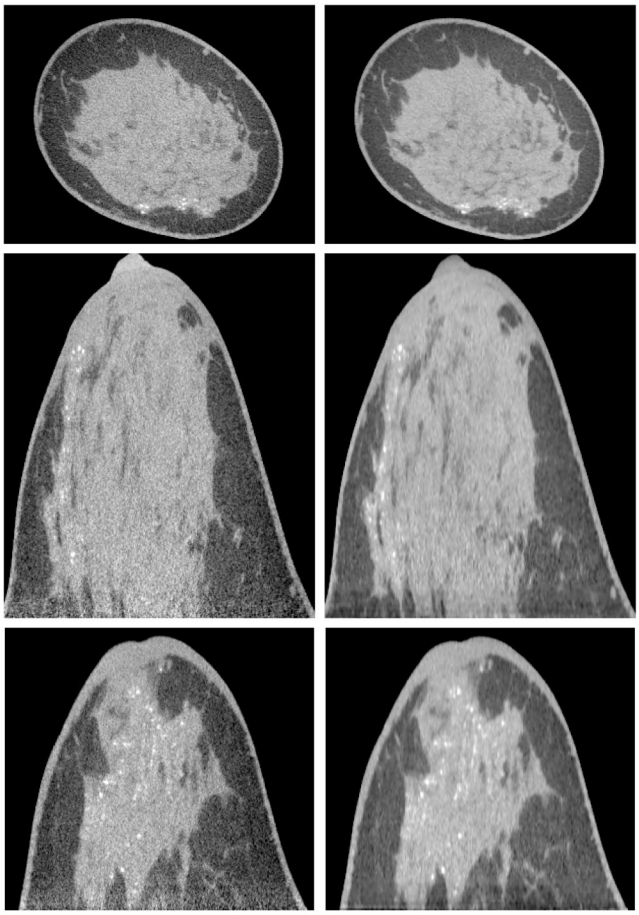

Figure 13.
Clinical FDK (left) and ASD-POCS (right) reconstructions within transverse (row 1), coronal (row 2), and sagittal(row 3) slices for the small-size breast. The display window is [0.15, 0.25] cm^{-1}.

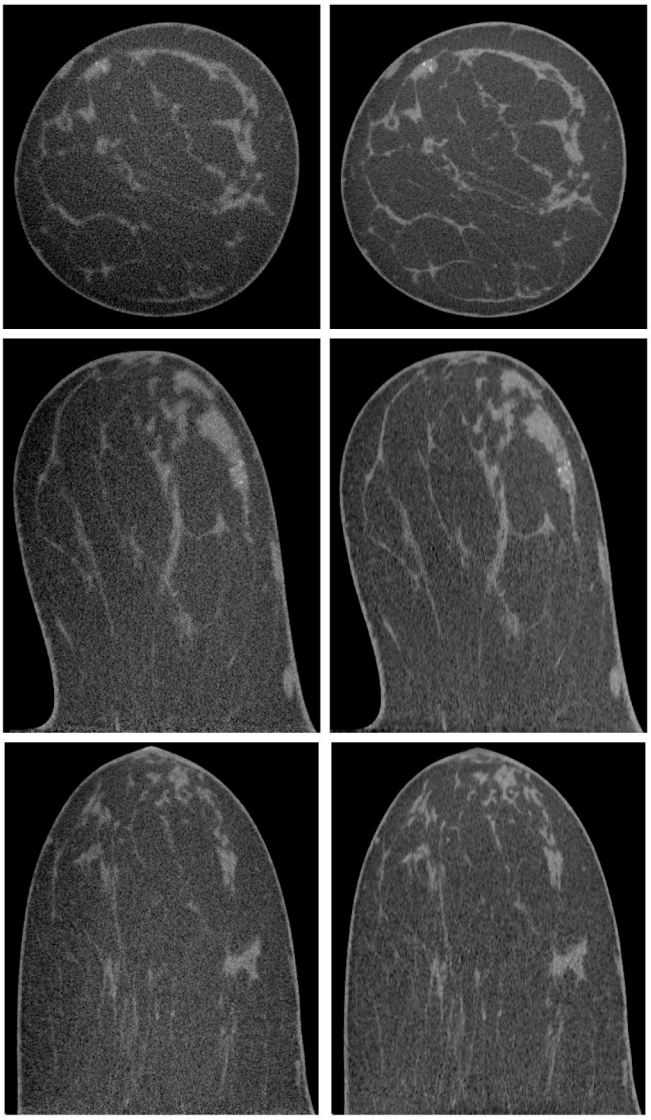

Figure 14.

Clinical FDK (left) and ASD-POCS (right) reconstructions within transverse (row 1), coronal (row 2), and sagittal(row 3) slices for the medium-size breast. The display window is [0.15, 0.30] cm^{-1}.

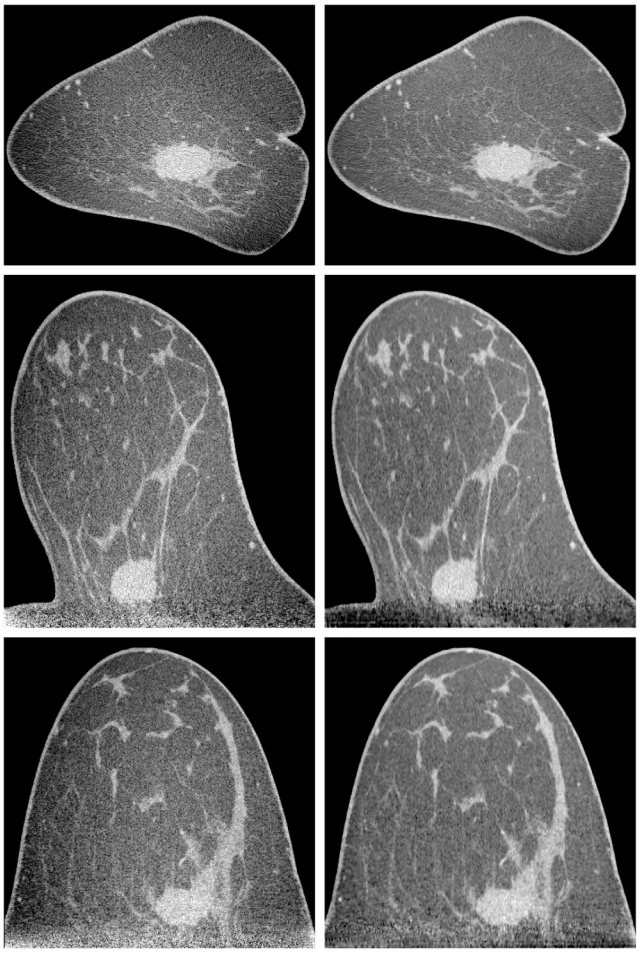

Figure 15.

Clinical FDK (left) and ASD-POCS (right) reconstructions within transverse (row 1), coronal (row 2), and sagittal(row 3) slices for the large-size breast. The display window is [0.15, 0.25] cm^{-1}.

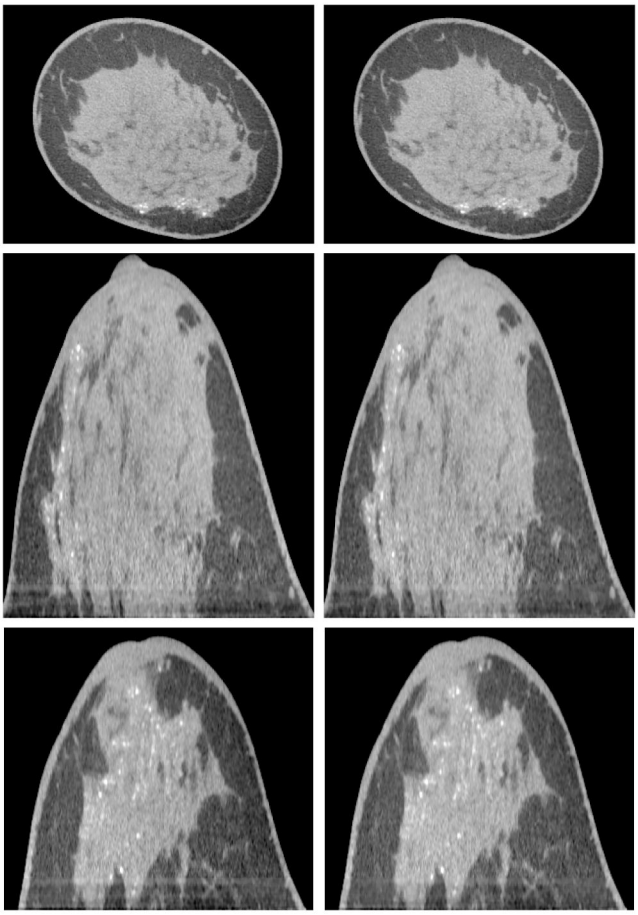

Figure 16.

ASD-POCS reconstructions at iterations 60 (left) and 80 (right) within transverse (row 1), coronal (row 2), and sagittal(row 3) slices for the small-size breast. The display window is [0.15, 0.25] cm^{-1}.

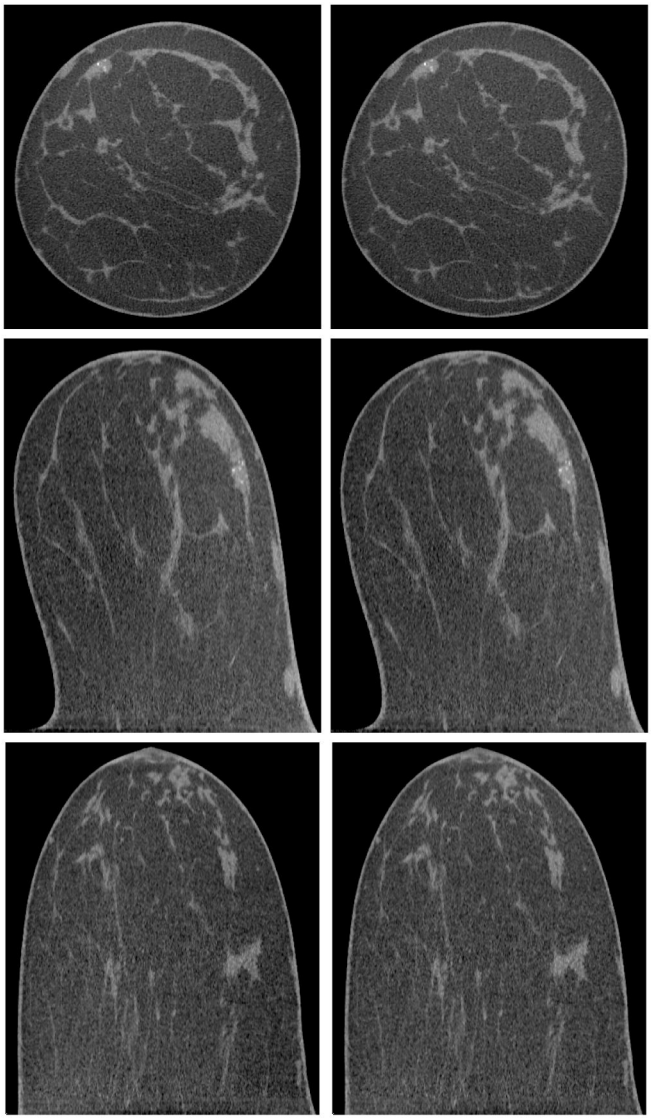

Figure 17.

ASD-POCS reconstructions at iterations 60 (left) and 80 (right) within transverse (row 1), coronal (row 2), and sagittal(row 3) slices for the medium-size breast. The display window is [0.15, 0.30] cm^{-1}.

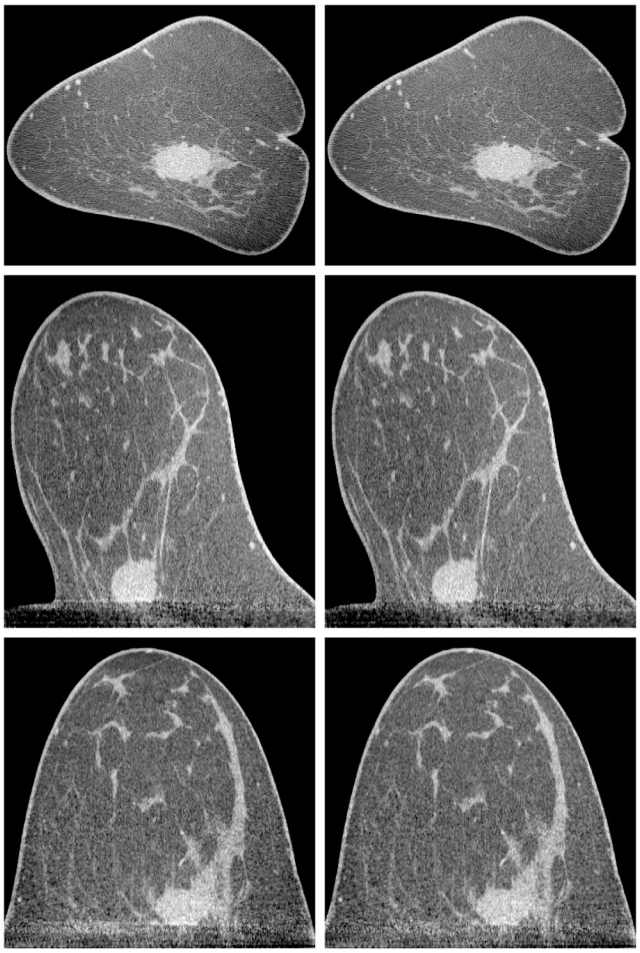

Figure 18.

ASD-POCS reconstructions at iterations 60 (left) and 80 (right) within transverse (row 1), coronal (row 2), and sagittal(row 3) slices for a large-size breast. The display window is [0.15, 0.25] cm^{-1}.

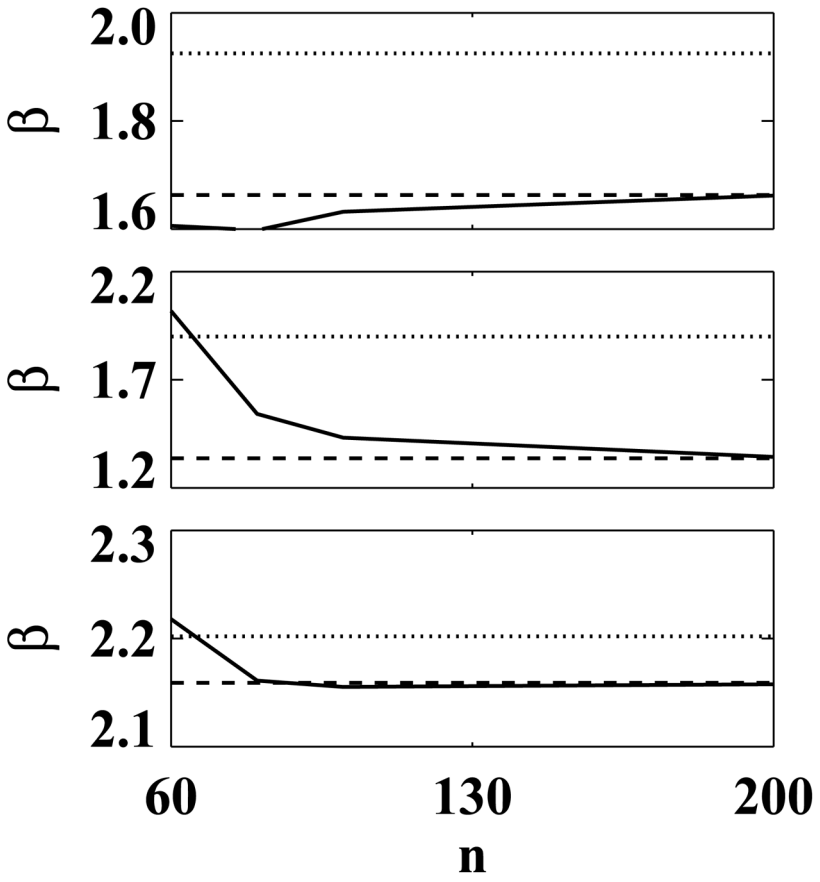

Figure 19.

Power-spectrum metric β as functions of iteration number n, along with those estimated from the convergent ASD-POCS reconstructions (dashed), for small- (row 1), medium- (row 2), and large-size (row 3) patient breast cases. Values of β estimated from the corresponding clinical FDK images (dotted) are plotted as benchmarking references.

Table I

Estimated power-spectrum metric β

β	Case 1	Case 2	Case 3
FDK	2.156	1.559	2.411
ASD-POCS	1.804	0.932	2.136

Table II

Estimated power-spectrum metric β

β	case 1	case 2	case 3
FDK	1.925	1.900	2.202
ASD-POCS	1.663	1.337	2.159